Photonics and Nanostructures - Fundamentals and Applications 62 (2024) 101326

Contents lists available at ScienceDirect

Photonics and Nanostructures - Fundamentals and Applications

journal homepage: www.elsevier.com/locate/photonics

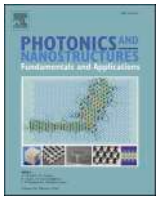

Tuneability and optimum functionality of plasmonic transparent conducting oxide-Ag core-shell nanostructures

Mohamed K. Zayed [a,b,*], Hesham Fares [a,c], Jamal Q.M. Almarashi [a], Samar Moustafa [a,c]

[a] Physics Department, College of Science, Taibah University, Medina 30002, Saudi Arabia
[b] Physics Department, Faculty of Science, Beni-Suef University, Beni-Suef 6111, Egypt
[c] Department of Physics, Faculty of Science, Assiut University, Assiut 71516, Egypt

ARTICLE INFO

Keywords:
Plasmonic transparent conducting oxide (TCO)
ITO-Ag and GZO-Ag core-shell nanostructures
Mie theory
Refractive index sensing
Solar energy harvesting
Geometrical optimization

ABSTRACT

Tunning localized surface plasmon resonance (LSPR) in transparent conducting oxides (TCO) has a great impact on various LSPR-based technologies. In addition to the commonly reported mechanisms used for tunning LSPR in TCOs (e.g., size, shape, carrier density modifications via intrinsic and extrinsic doping), integrating them in core-shell structures provides an additional degree of freedom to expand its tunability, enhance its functionality, and widen its versatility through application-oriented core-shell geometrical optimization. In this work, we explore the tuneability and functionality of two TCO nanostructures; indium doped tin oxide (ITO) and gallium doped zinc oxide (GZO) encapsulated with silver shell within the extended theoretical Mie theory formalism. The effect of core and shell sizes on LSPR peak position and line width as well as absorption and scattering coefficients is numerically investigated. Simulations showed that LSPRs of ITO-Ag and GZO-Ag core-shell nanostructures have great tunning capabilities, spanning from VIS to IR spectral range including therapeutic window of human tissue and essential solar energy spectrum. Potential functionality as refractive index sensor (RIS) and solar energy absorber (SEA) are examined using appropriate figure of merits (FoM). Simulations indicate that a geometrically optimized core-shell architecture with exceptional FoMs for RIS and SEA can be realized. Contrary to carrier density manipulation, integrating TCO cores to metallic shells proves to be an effective approach to enhance tunability and optimize functionality for high performance TCO-based plasmonic devices, with minimum impact on the inherited physical and chemical properties of the used TCO-core materials.

1. Introduction

Extrinsic semiconductor nanomaterials (NMs) are proven to be Drude-type non-metal plasmonics that have attracted great interest due to its tunable properties in the near-infrared (NIR) range, and potential role in the development of new types of nano-optical devices [1–5]. Localized surface plasmon resonance (LSPR) in these NMs results in resonant scattering, absorption and near field enhancement around NM particulates [6,7]. LSPR in these semiconductor plasmonics can be tuned across a wide optical range, from visible (VIS) to far-infrared, by varying doping level and post syntheses treatment in addition to commonly used tunning parameters for traditional Au and Ag plasmonic NMs; e.g., size, size-distribution, shape, and external environment [1–12]. An addition important fact is that the absorption losses in such plasmonic semiconductor NMs in VIS range are normally much lower than those in noble metal plasmonic NMs [5,7,11]. Also, it exhibits considerable thermal and environmental stability as well as low coast and easy preparation [5,12,14]. Over the past decades, researchers have achieved precise control sizes, shapes and dopant of semiconductor nanostructures using various synthesis techniques tackling good LSPR criteria of low optical loss, heavily dopped and negative dielectric constants [6–25]. These above-mentioned merits make semiconductor plasmonic NMs not only good alternative candidates to replace traditional noble metals in some applications, but also to be integrated with noble metals to pertain a wider application range in various advanced photophysical- and photochemical- based applications with enhanced performance [6–12].

Transparent conducting oxides (TCO) such as indium doped tin oxide (ITO) and gallium doped zinc oxide (GZO) are among oxide semiconductor NMs that have been considered for various plasmonics applications in the NIR range [13–16]. Resonating charges in these TCOs can be tailored to highly degenerate doping states either intrinsically via

* Corresponding author at: Physics Department, College of Science, Taibah University, Medina 30002, Saudi Arabia.
E-mail address: mkzayed@outlook.com (M.K. Zayed).

https://doi.org/10.1016/j.photonics.2024.101326
Received 14 August 2024; Received in revised form 13 October 2024; Accepted 5 November 2024
Available online 8 November 2024

controlling lattice defects or extrinsically via foreign atoms doping [6–17]. Thus, its permittivity can be flexibly engineered resulting in an epsilon near-zero behavior with a tunable spectral range from VIS to far IR [16–18]. In otherwards, well-controlled LSPRs absorption band of TCOs can be fashioned by manipulating material's properties such as electron density, dielectric constant, and the dielectric constant of the surrounding medium as well, which can be contributing significantly in plasmon science and applications [19,20]. Kanehara et al. utilized solution-phase chemical synthesis to synthetized high-quality ITO nanocrystals with an adjustable LSPR that can be tuned from 1618 nm to >2200 nm by controlling the Sn concentration [19]. Nevertheless, relative to gold that was easily electrochemically oxidized, ITO showed excellent stability and withstand voltages of >1000 V in solution or polymer films [19]. Experimental measurements packed by theoretical modeling simulations showed that LSPR of ITO nanostructures can be varied through careful patterning and post synthesis treatment, and also demonstrated a shift in the LSPR frequency as a result of changing the refractive index of the surrounding medium [21]. Ma et al. reported that the LSPR of monodispersed ITO NPs can be adjusted from 1600 to 1993 nm by controlling the dopant concentration, the size, and the shape of ITO NPs [22]. Della Gaspera et al. developed a method to synthesis colloidal monodispersed GZO nanocrystals of over 15 % atomic doping levels and a tailored NIR LSPR plasmonic absorption band [23,24]. Ga doping extends the optical response range of ZnO devices to NIR region showing strong absorption in the UV–VIS–NIR band (365–1064 nm) [25]. Nano-triangle GZO arrays fabricated by nanosphere lithography and pulsed laser deposition also showed a similar LSPR behavior that can be tuned in IR region by controlling both Ga doping concentration and crystallite sizes [26]. Monitoring the peak shift of the NIR LSPR induced by degenerately doped GZO nanocrystal thin films have been utilized to detect both oxidizing and reducing gases (H_2 and NO_2) at mild (<100 °C) operating temperatures [27]. Moreover, by exposing the GZO film to blue light during sensing measurements, a room temperature sensitivity to sub-ppm of NO_2 concentrations could be achieved [27].

Because of the wide tunable LSPR-spectral range of TCO NMs, exploring its plasmonic properties remains of great relevance to numerous plasmon-based applications [6–12]. Its tunable range coincides with solar spectrum (250–2500 nm) and hence is appropriate for smart windows, solar energy harvesting, and waste heat management applications [5–7]. It also overlaps with therapeutic window of human tissue; hence is suitable for photothermal therapy and bio-imaging [2–12]. While doping is considered as a powerful tool for controlling carrier concentration in TCO NMs and hence its LSPR response, it leads to a notable deterioration in free electron mobility due to the increased scattering probability with ionized dopant atoms or with the produced defects [17–26]. This process also broadens the LSPRs and weakens the opportunity for strong near-field enhancement. In addition, compositional changes via introducing high concentrations of impurity atoms can induce changes in its electric, electronic, and thermal properties as well as its crystal structure relative to its counter pure stochiometric structure [28,29]. Finally, when approaching higher carrier concentration via chemical doping, the solubility limit of the dopant might become a limiting factor [27–29]. Thus, it is of considerably important to tune and tailor the LSPR of TCOs NMs with minimum impact on the inherited physical and chemical properties.

Integrating two or more materials with different properties and different functionality into single hybrid nanoparticles (NPs) with designed properties has become increasingly desirable for wider application prospects and enhanced performance [30–32]. Core–shell configuration is one of these hybrid nanostructures in which an internal core is encapsulated by a shell of another material. Relative to single element plasmonic NMs, the LSPR properties of core–shell nanostructures depend on not only the size, shape, and local environment, but also on relative core–shell compositions and geometries. Core–shell nanostructures with various compositions including metallic cores and metallic shells (bimetallic nanostructures) [30,31], metallic cores and an oxide shells [32,33], and semiconductor cores with metallic shells [32–34] have been explored. For plasmonic materials, the hybrid plasmonic response supported by the inner and outer surfaces of core–shell nanostructures provides not only a remarkable tuneability but also a wider functionality of the core-shell nanostructure [30–34]. Tam et al. have theoretically and experimentally investigated the refractive index sensitivity (RIS) of SiO_2–Au core–shell systems, demonstrating enhanced LSPR-based sensitivity [35]. Furthermore, AZO-Au and GZO-Au core--shell nanostructures demonstrated a remarkable enhancement in hyperthermia efficiency, surpassing SiO_2 by multiple orders of magnitude, under identical conditions [36]. With anticipated enhanced sensitivity and better surface enhanced Raman scattering, Hong et al. studied the effect of coupling ITO and TiO_3 deposits to plasmonic Ag thin films [37].

The coupling of plasmonic materials in core–shell nanostructures is an effective approach to respond to the current sophisticated industrial and technological material demands for advanced state–of–the–art device fabrications and future needs. While the plasmonic properties of TCO have been experimentally and theoretical investigated, integrated them in core-shell nanostructure and its geometrical optimization have been rarely addressed. Furthermore, surface defect states and trap states as well as possible attached molecules have been reported to alter the electronic structure near the surface of spherical TCO nanocrystals, leading to the formation of a depletion layer with reduced charge carrier density compared to its inner central density [3,11,38,39]. This depleted layer shields the active TCO plasmonic center, affecting its properties such as sensitivity and near-field enhancement. The depletion effect decreases with larger nanocrystal size and higher doping levels [3,11,38]. Minimizing depletion effects e.g.; encapsulating TCO core with metallic shell, could be a promising approach for improving its sensitivity and enhancing its functionality. In this work, the optical properties and functionality of some spherical TCO-metal core-shell nanostructures are investigated using Mie theory formalism. Here, ITO and GZO are used as typical TCO material examples. The fundamental photonic properties of these TCO-Ag nanoshells are studied to explore the effect of core and shell sizes on its optical response for geometrical optimization and potential functionality. Both absorption (Q_{abs}) and scattering (Q_{abs}) coefficients are simulated for various core and shell sizes. It is demonstrated that Q_{abs} increases with effective particle volume up to a size above which Q_{sca} becomes dominant; giving an opportunity to be utilized in either absorption-dominant or scattering-dominant regime. Potential functionality as RIS and solar energy absorber (SEA) are examined using appropriate figure of merit (FoM). Relative to single spherical particles counterparts, these systems showed a wide range of LSPR tunability that spans from VIS to MIR. In addition, via meticulous geometric optimization of the core and shell sizes, these optimized nanoshell structures exhibit exceptional FoM as RIS and SEA functional nanostructures, with values surpassing several currently available plasmonic nanostructures. This work shades the light on the capabilities of adapting TCO-metallic core-shell architectures as an effective approach to enhance tunability and optimize functionality, with minimum impact on the inherited physical and chemical properties of the used TCO-core materials.

2. Theory and simulations

The theoretical formalisms of Aden and Kerker [40,41], based on the Mie theory, are employed to calculate the plasmon spectra of spherical TCO-Ag nanoshell structures. In the original Mie theory, the internal and external (scattered) electromagnetic (EM) fields inside and outside an isotropic homogenous spherical particle are expressed as an expansion of a series of vector spherical harmonics representing the normal modes of the EM field which satisfy the boundary conditions at the particle-medium interface [42]. Following the same methodology of Mie theory, Aden and Kerker developed a general analytical solution to Maxwell's equations that describes the scattering and absorption of the

EM field by a layered nanoparticle or a concentric core and shell spheres [40,41]. Refractive indices and dielectric characteristics of the core and shell materials are arbitrary. Fig. 1 depicts the incident plane wave and the scattering configuration with respect to spherical coordinates taking the origin to be at the center of the core-shell nanospheres. The incident plane wave is propagating in the positive z direction, and its electric vector is linearly polarized in the x direction. The EM field in the nanoshell regions (i.e., core, shell, medium) can be determined by Mie-like coefficients denoted by a_n and b_n. The scattering and extinction coefficients are expressed by [40,41]

$$Q_{\text{sca}} = \left(\frac{2}{\alpha^2}\right)\sum_{n=1}^{\infty}(2n+1)\left[\text{Re}\left(|a_n|^2+|b|^2\right)\right] \tag{1}$$

$$Q_{\text{ext}} = \left(\frac{2}{\alpha^2}\right)\sum_{n=1}^{\infty}(2n+1)[\text{Re}(a_n+b_n)] \tag{2}$$

where $\alpha = 2\pi(R_s/\lambda)$ is the size parameter, λ is the wavelength of light, and R_s is the particle radius projected onto a plane perpendicular to the incident beam (i.e., R_s is the outer radius of a spherical nanoshell). With the help of Eqs. (1) and (2), the absorption coefficient is given by $Q_{\text{abs}} = Q_{\text{ext}} - Q_{\text{sca}}$.

As part of the ongoing numerical simulation effort, we developed a Mathcad code employing Toon and Ackerman's algorithms [43,44]. A complete description of the parameters a_n and b_n shown in Eqs. (1) and (2), composed of Riccati-Bessel functions and their derivatives, have been reported in [43]. Our code demonstrates a very good match with previously reported experimental data for absorption and scattering efficiencies for a wide variety of core-shell materials [44].

It is worth mentioning that TCOs, particularly ITO and GZO, have an almost energy band alignment with Ag due to their comparable work functions; $\Phi_{Ag} \approx 4.4eV$, $\Phi_{ITO} \approx 4.5-5.1eV$ and $\Phi_{GZO} \approx 4.23-4.4eV$ (variations in Φ_{ITO} and Φ_{GZO} are due to the sensitivity of the measuring technique toward surface treatment and/or adsorbates) [45,46]. These almost band alignments allow for small electron transfer between Ag and adjacent TCO layer with insignificant interfacial barrier. In fact, TCO/metal/TCO multilayer films including ITO/Ag/ITO, AZO/Ag/AZO and GZO/Ag/GZO have been utilized as solar cell electrodes of superior performance, compared to single-layer electrodes, in terms of achieving low resistance and high transmittance values at reduced film thicknesses [47]. The superior electric and optical performance of such multilayer interfacial structural electrodes indicate the dominant ohmic behavior and/or insignificant Schottky barrier effect. In otherwards, these proposed TCO-Ag core-shell nanostructures not only are experimentally feasible, but form composition structures with insignificant interfacial effects that might affect the accuracy of our calculations regardless to the structure mismatch and different cohesive energies. In the numerical simulations, we employ the Drude–Lorentz parameters reported in [48] since they provide an accurate description of the experimental dielectric permittivity of TCOs (i.e., GZO (6 wt%) and ITO (10 wt%)) in the 350–2000 nm spectral region. When using other Drude-Lorentz parameters, published in literatures to describe different dielectric permittivity measurements [4,5], no discernible difference in the results of this paper is found. The dielectric function of the TCO core, considering the plasmon damping caused by electron scattering at the core surface, is given by

$$\epsilon(r_{\text{eff}},\omega) = \epsilon_\infty - \frac{\omega_p^2}{\omega(\omega+j\Gamma_{\text{mod}})} - \frac{m_1\omega_1}{\omega_1^2-\omega^2-j\omega\Gamma_1} \tag{3}$$

where ϵ_∞ is the permittivity at infinite frequency (background permittivity), ω_p is the plasma frequency, m_1 is the amplitude of the Lorentz oscillator with principal frequency ω_1 and damping rate Γ_1. Γ_{mod} is the modified bulk collision frequency due to the size-dependent electron scattering such that;

$$\Gamma_{\text{mod}} = \Gamma_0 + A\frac{v_f}{r_{\text{m}}} \tag{4}$$

Γ_0 is the bulk TCO damping constant, r_{m} is the maximum possible mean free path of electrons for collisions with the boundary (i.e.,$r_{\text{m}} = 2R_c$ for the core region and $r_{\text{m}} = d$ for the shell region), and v_f is the Fermi velocity. In Eq. (4), the effective mean free path of electrons is $r_{\text{eff}} = r_{\text{m}}/A$ where A is a proportionality constant between r_{eff} and r_{m}. In this study, A is assumed to be 1 [49]. Overall, the electron concentration n_e in the TCOs is in the range of $(10^{20}-10^{21})$ cm^{-3} [7,50,51], while the effective mass of an electron m_e^* is approximately in the range of $(0.3-0.7)m_e$. For instance, m_e^* of GZO and ITO equals $0.4m_e$ [52], and $0.35m_e$ [51] when $n_e = 10^{21}\text{cm}^{-3}$, respectively. By embedding these values in the fermi velocity $v_f = (\hbar/m_e^*)(2\pi n_e)^{1/2}$, one finds that the damping rate due to the surface scattering ($v_f/2R_c$) has a negligible effect in comparison to the electron scattering in the bulk Γ_0 (for TCO materials $\hbar\Gamma_0 \sim$ 0.1 eV) when $R_c \geq 3$ nm. In this study, the relaxation rate of electron-surface collisions can be neglected for the assumed range of the used core radius. The parameters of the Drude-Lorentz model shown in Eq. (3) for ITO (10 wt%), GZO (6 wt%) as reported in [48], $\epsilon_\infty = 3.528$ and 2.475, $\omega_p = 1.78$ eV and 1.927 eV, $\hbar\Gamma_0 =$ 0.155 eV and 0.117 eV, $m_1 = 0.388$eV and 0.866 eV, $\hbar\omega_1 = 4.210$ eV and 4.850 eV, and $\hbar\Gamma_1 = 0.092$ eV and 0.029 eV, respectively.

The dielectric function of metallic shell (Ag shell) is also determined by the Lorentz-Drude theory using notations identical to those in Eq. (3) [52,53], being given by

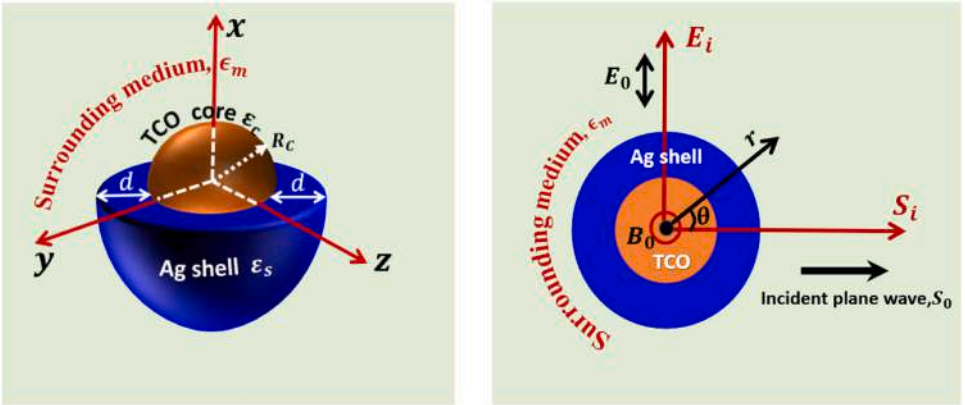

Fig. 1. In the left panel, a schematic illustration of concentric TCO-core and Ag-shell spheres embedded in a surrounding medium where R_c is the core radius and d is the shell thickness. ϵ_c, ϵ_s, and ϵ_m denote the dielectric function of the core, shell, and embedding medium, respectively. The right panel illustrates the propagation of an incident plane wave with an intensity $\boldsymbol{S}_0$ in the positive $z-$ direction while its electric field vector $\boldsymbol{E}_0$ is linearly polarized in the $x-$ direction.

$$\epsilon(r_{\text{eff}},\omega)=\epsilon(\omega)_{\text{exp}}+\frac{\omega_p^2}{\omega^2+j\omega\Gamma_0}-\frac{\omega_p^2}{\omega^2+j\omega\Gamma_{\text{mod}}} \quad (5)$$

In Eq. (5), $\epsilon(\omega)_{\text{exp}}$ is the experimental bulk dielectric function, and can be accurately given by [53]

$$\epsilon(\omega)_{\text{exp}}=1-\frac{\Omega_p^2}{\omega^2+j\omega\Gamma_0}+\sum_{j=1}^{N}\frac{m_j\omega_p^2}{\left(\omega_j^2-\omega^2\right)-j\omega\Gamma_j} \quad (6)$$

where $\Omega_p=\sqrt{f_0}\omega_p$ is a plasma frequency associated with intraband transitions with oscillator strength f_0 and damping constant Γ_0. The contribution of interband transitions to the dielectric function is represented by the third term on the right-hand side in Eq. (6) where m_j denotes the number of oscillators having frequency ω_j, strength f_j, and lifetime $1/\Gamma_j$. In this study, we use the values of the Lorentz-Drude parameters shown in Eqs. (5) and (6), as reported in [53].

3. Results and discussion

3.1. Tunability of TCO nanosphere and nanoshells

It is well known that the optical properties of a plasmonic particle are strongly dependent on its size and shape [3–7,22]. LSPR features of a single spherical plasmonic particle are influenced by changing the particle size, including the wavelength of the LSPR resonance peak (λ_r), peak intensity and full width at half maximum (FWHM) as well as the field distribution of plasmon modes. This is mainly due to the increase in the effective volume of the particle that alters the materials' polarizability and hence the plasmon resonance as well as their scattering/decaying mechanisms. In general, small particles show only dipolar modes at frequency close to the conductor's plasma frequency, while larger particles show relatively wider red-shifted dipolar peaks [3–7,17,18]. In addition, larger particles can also show higher order plasmon resonance modes arising from different arrangements of its resonating electrons in response to the incident light. All such effects are precisely described by our adopted Mie theory formalism [37,42,55]. Fig. 2 and its insets show the effect of the variation in the particle radius R_c on the absorption coefficient Q_{abs} of single plasmonic Ag, ITO and GZO particles as calculated for vacuum or air surrounding medium ($n_{med}=1$). For the smallest investigated particle size ($R_c = 10nm$), Ag plasmonic NPs exhibit a resonance peak at ∽390 nm corresponding to the blue to orange region of the visible spectrum, while ITO and GZO show resonance peaks in the NIR region at ∽1690 nm and ∽1490 nm, respectively. If considering an aqueous surrounding medium of higher refractive index ($n_{\text{med}} = 1.33$), λ_r of Ag, ITO and GZO plasmonic nanospheres shift to longer wavelengths, red-shifted, to be 426, 1896 and 1686 *nm* for Ag, ITO and GZO nanospheres, respectively, which is also accompanied by an increase in absorption intensity and a narrowing in the absorption peaks. This is because a higher refractive index medium allows for more efficient coupling of the incident light to the plasmonic oscillations, leading to a stronger and sharper LSPR response [8,11,14,22,33]. These obtained values of λ_r for these plasmonic nanospheres are consistent with previously reported theoretical and experimental investigations of comparable sizes for vacuum and/or aqueous surrounding mediums [4,13,19,21,22,26,28,48]. As the particle radius increases from 10*nm* to 60*nm*, these single plasmonic nanospheres exhibit small red shift in their peak positions showing a limited size-dependent tunability; $\Delta\lambda$ ∼20–50 nm width within the considered variation range of particle radius (from 10 to 60*nm*), regardless to the surrounding medium. In addition, it is worth noting that higher-order plasmonic effects e.g., electric quadrupole modes, start to appear in the absorption spectra of Ag nanosphere at $R_c \geq 50$ nm. Such higher-order effects are not observed for plasmonic TCOs single nanospheres within the investigated spherical radius range and for the wavelength range assumed in the calculations. Higher order modes are not expected in 60 nm ITO and GZO nanospheres, because this size is small compared to their LSPR wavelengths (∼1500 nm).

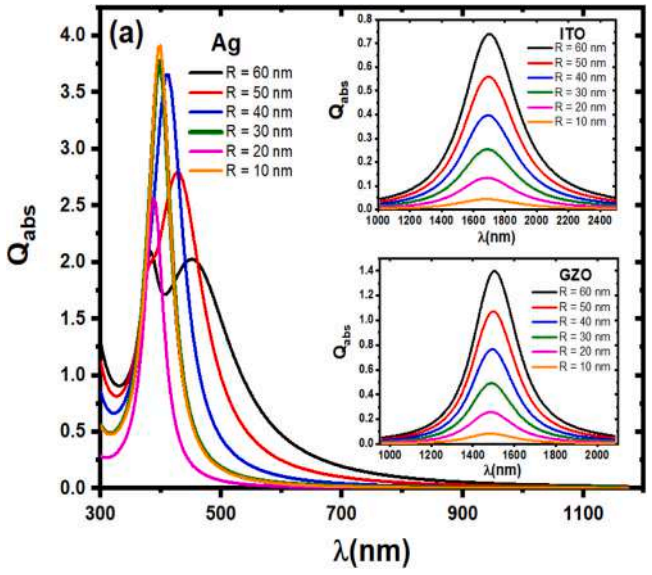

Fig. 2. The effect of the particle radius (R) on the calculated absorption coefficient (Q_{abs}) of single plasmonic Ag, ITO and GZO, assuming air surrounding medium ($n = 1$).

In contrast to single plasmonic nanospheres where LSPR can be tuned primarily by changing their size, the LSPR of plasmonic nanoshells can be tuned by varying both the core radius (R_c) and the shell thickness (d). Fig. 3(a) and (b) show the effect of shell thickness on Q_{abs} and Q_{sca} of ITO − Ag and GZO − Ag nanoshells as calculated at constant core radius ($R_c = 40nm$) and aqueous surrounding medium ($n_{med} = 1.33$). By increasing the shell thickness, both ITO − Ag and GZO − Ag nanoshells show very strong tunning abilities that extend from NIR to VIS, as shown in Fig. 3. The peak positions of the absorption spectrum of ITO − Ag and GZO − Ag nanoshells are intensified, narrowed, and shifted toward lower wavelengths, blue shifted, as d increased. However, Q_{sca} is intensified and broadened with increasing d. At $d = 8nm$, an absorption shoulder corresponding to Ag-higher plasmonic modes start to appear and continue to intensify and blue shifted with further increase in the shell thickness d. In addition to the appearance of the Ag higher order plasmonic modes, the ability of the plasmonic ITO − Ag and GZO − Ag nanoshells to scatter incident light becomes more pronounced. In otherwards, Q_{sca} increases on the expense of a relative decrease in Q_{abs} suggesting a very strong geometrical tuning dependent as well as geometrical optimization and tradeoff between absorption and scattering characteristics of these plasmonic nanoshells. This means that a larger fraction of the incident light is scattered by the nanoparticles, rather than being absorbed or transmitted at that composition. The increased scattering coefficient leads to more efficient coupling of the incident light to the far-field, allowing the plasmonic NPs to interact with and influence the propagation of light over longer distances, which results in an enhanced light-scattering patterns, interference effects, and hence improved optical sensing and detection [40,41,43].

Fig. 4 shows the results of our systematic investigations of the fundamental tuning ability of TCO − Ag nanoshell structures; where the variations of λ_r for ITO − Ag and GZO − Ag nanoshell structures of different values of core radius R_c and shell thickness d (up to $d = 20nm$) for water surrounding medium ($n_{\text{med}} = 1.33$) are investigated. It is clear that λ_r of these TCO − Ag nanoshells decreases almost exponentially from NIR range, corresponding to the single TCO nanosphere, to almost VIS (almost blue) with increasing the value of d in the TCO − Ag nanoshells depending on R_c. For $R_c = 20nm$ and d is varied from 0 to 20 *nm*, λ_r of ITO − Ag decreased from 1890 to 517 nm and that of GZO − Ag decreased from 1690 to 518 *nm*. This indicates a great tunning

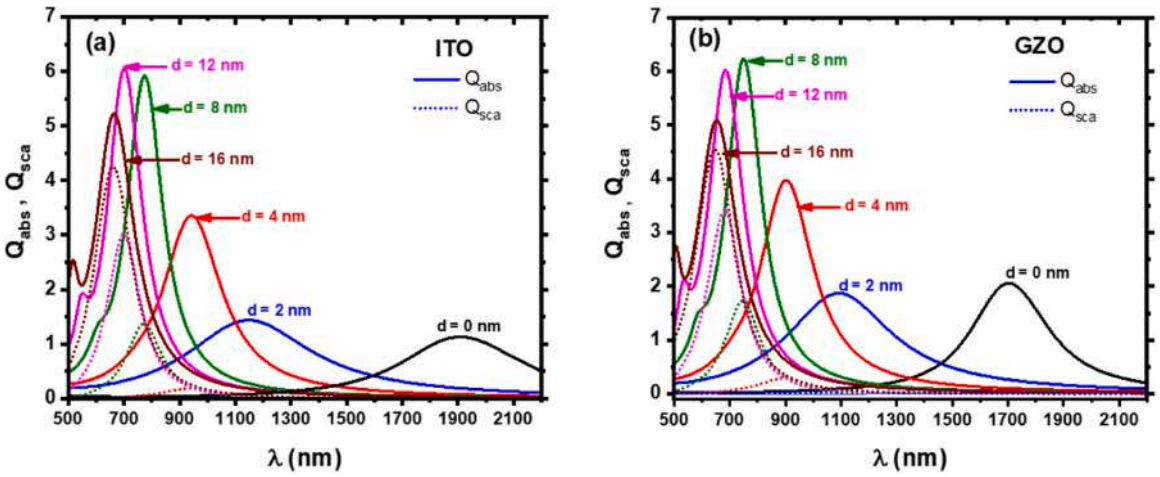

Fig. 3. The simulated absorption coefficient (Q_{abs}) and scattering coefficient (Q_{sca}) spectra of TCO-Ag nanoshells; **(a)** ITO-Ag nanoshell and **(b)** GZO-Ag nanoshell. The spectrum is calculated at constant core radius of 40 nm and at different Ag shell thickness assuming an aqueous surrounding medium ($n_{med} = 1.33$).

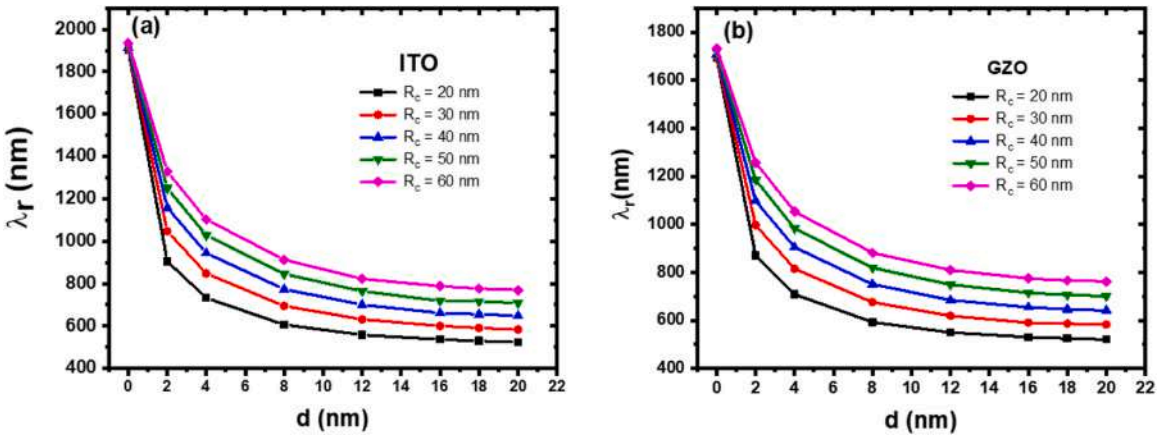

Fig. 4. Variation of the resonance wavelength (λ_r) of TCO-Ag nanoshell structures with various core and shell sizes: **(a)** ITO − Ag nanoshell and **(b)** GZO − Ag nanoshell.

ability of total tunning range $\Delta\lambda \sim 1340$ and 1170 nm for ITO − Ag and GZO − Ag nanoshells, respectively. Regarding the tunability range, the tunning range of ITO − Ag and GZO − Ag nanoshells is larger than that observed due to Sn or Ga doping in ITO and GZO. Kanehara et al. was able to tune LSPR in colloidal ITO nanocrystals from 1618 nm to >2200 nm with tunning range of $\Delta\lambda \approx 600$ nm by controlling the Sn concentration between 0 % and 40 % [19]. Controlling the free carrier due to Ga doping in GZO was reported to tune LSPR peak position from 4000 nm to 3000 nm [12]. However, X. Ye et. al used a generalized cation−anion co-doping methodology to tune the LSPR of ITO nanocrystals between 1.5 and 3.3 μm showing a larger tunning range of $\Delta\lambda \approx 1800nm$ [18]. H. Long et al. also reported tunning range of $\Delta\lambda \approx$ 1200 nm (from 2.4 to 3.6 μm) of Al and Ga co-doped ZnO (AGZO) nano-triangle particulates by changing the doping concentrations [56]. Despite of the wide tunable range due to this co-doping approach, it obviously alters the composition and the intrinsic dielectric properties of the TCO material itself in addition to several raised issues that might degrade the performance of any plasmonic based devices raised from the increased formed defect density and/or ineffective doping due to solubility limits, as well as increased ionized impurity scattering [15,27–29]. In addition, the LSPR tunability due to doping, red shifts λ_r toward IR range while our TCO-metal integration tunning approach blue shifts λ_r toward VIS and UV range. In any instant, this doping tunning recipe can be considered as an additional strong bonus to the current approach since TCO cores with any arbitrary and experimentally attainable doping concentrations can be integrated to a suitable metallic shell for even wider LSPR tuning range. These TCO-metal nanoshell structures have potential tunning ability that by far surpasses metal-metal, metal-semiconductor, semiconductor-metal core-shell nanostructures [28, 57–59]. In fact, this wide LSPR tunability range of TCO-metal nanoshell structures allows for designing plasmonic devices that can operate at any desirable wavelength within such wide tuning range, which gives flexibility in the design and engineering of various plasmonic-based devices. It is worth noting that, TCO-Ag core-shell configuration, in its optical behavior, is closer to bimetallic core-shell rather than dielectric-metal core-shell configuration. TCOs have very broad LSPR spectrum that expands over VIS-NIR-MIR range due to its available high doping-dependent free carrier concentrations and the inherited electron-impurities and electron-defect scattering mechanisms [3,4,7, 11,17]. Metallic NPs normally have narrow and sharp LSPR spectrum in the VIS range [8,54]. The current TCO-Ag core shell structure resembles bimetallic in the sense that the IR broad LSPR spectrum of ITO and GZO are modulated by a varying metallic-shell thickness resulting in a hybrid modified blue shifted spectrum. The TCO-Ag LSPR spectrum continues to be blue shifted and narrowed reaching the edge of the VIS range at larger Ag-shell thickness. In otherwards, LSPR are tuned continuously from the dipolar resonance of ITO and GZO single spheres in the NIR range to the resonance of Ag at the blue edge of the VIS range. Similar behavior commonly observed for bimetallic core shell structures, but with limited modifying range (within the VIS region only) and narrower

FWHM [30,31,57,59].

3.2. Geometrical optimization and functionality

As mentioned above, TCO-Ag nanoshells have shown wide LSPR tunability range inheriting them a great design flexibility and enables for the realization of multifunctional plasmonic devices. These devices can integrate various functionalities, such as sensing, energy conversion, and optical control, within a single platform or can be geometrically optimized to achieve an optimum desired performance for specific application. However, this geometrical optimization and design process normally involves complex trade-offs amonge various controlling or functionality parameters such as scattering, absorption and transperancy. Fig. 5 shows the absorption and scattering coefficients at resonance,$(Q_{abs})_r$, for ITO − Ag and GZO − Ag nanoshells calculated at various core and shell sizes and aqueous surrounding medium. It is clear that $(Q_{abs})_r$ increases with increasing the shell thickness d, till it reaches a maximum at shell thickness d_m, after which $(Q_{abs})_r$ starts to decrease with further increase in d. This behavior is observed for both ITO − Ag and GZO − Ag nanoshells. For small core sizes ($R_c = 20$ and 30 nm), the maximum in $(Q_{abs})_r$ is observed at d_m located between 12 and 16 nm for both TCO − Ag nanoshell structures. However, at higher core radius ($R_c > 30\ nm$), R_C independent maximum in $(Q_{abs})_r$ is observed at $d_m \approx 8\ nm$. The scattering coefficient at resonance, $(Q_{sca})_r$ exhibits nonlinearly increase with increasing d throughout the investigated range. However, it pertains a lower increasing rate at higher values of d; particularly for higher values of R_c. While a maximum of $(Q_{abs})_r$ is observed within the investigated range of core and shell sizes, $(Q_{sca})_r$ have its maximum value slightly larger or beyond these ranges; at lower values of R_c. The consensus is that Q_{abs} increases with effective particle volume up to a size above which Q_{sca} becomes dominant. Thus, one can manipulate the geometrical parameters of these TCO-Ag nanoshell structures to utilize the optimum absorption and/or optimum scattering characteristics i.e., it can be geometrically optimized to operate either in absorption- or scattering-dominated regime. Whereas absorption-dominated regime is desirable for photothermal therapy, photocatalysis, and solar energy harvesting, scattering-dominated regime is advantageous for applications such as optical sensing, imaging, and optical switching. Based on these results, TCO-Ag with relatively small TCO cores and small Ag shells ($d < 12$ nm) can be utilized for absorption-dominated applications while those with large TCO cores and large Ag shells ($d > 12$ nm) can be utilized for scattering-dominated applications. In plasmonic-based enhanced solar cells, Q_{abs} and Q_{sca} are believed to be equally important as effective approaches to strategically maximize light absorption and/or trapping [60]. Manipulating absorption and scattering components using plasmonic NPs have previously exploited to enhance efficiencies of photovoltaic solar cells adapting different photoelectron generation mechanisms [61,62]. Whereas Q_{abs} of plasmonic NPs can provide an enhanced broadband spectral absorption of the solar spectrum added to that naturally absorbed by active medium, Q_{sca} of embedded plasmonic NPs can be utilized to capture light photon within the active medium via wide angel scattering or antireflecting-like mechanisms; an approach usually obtained by surface texturing [60]. Incorporating plasmonic NPs between the hole transport layer and the active layer was reported to significantly increase light absorption and scattering, leading to higher power conversion efficiency [61,62]. It has been demonstrated that the placement of these plasmonic NPs (at surface of the front or back electrodes or embedded among/within active layer) plays a crucial role in improving light absorption, scattering, and electrical properties facilitated by these incorporated plasmonic NPs [60–62]. Thus, absorption peak tunability of these TCO-Ag nanoshell can enhance photoelectron conversion efficiency via widening the absorbed solar spectrum and the effective formation of hot electrons, which can be drifted toward the solar cell active layer providing an enhanced solar energy conversion. In addition, such plasmonic nanoshells can be embedded within the active medium where the scattered light from plasmonic NPs is trapped allowing for an improved photoelectron generation, and a higher solar cell efficiency.

The FWHM of the LSPR peak is of crucial consideration during geometrical design optimization; either in absorption-dominated or scattering-dominated regime [63,64]. Generally speaking, a narrow FWHM of the LSPR peak, i.e. sharp resonance, allows for high spectral selectivity, which is importante for applications that require precise wavelength-dependent interaction such as chemical and biological sensing [1,19,33,42,59]. In that context, the FWHM is inversely related to the sensitivity of plasmonic sensors, as a narrower FWHM allows for the detection of smaller shifts in the resonance wavelength due to changes in the local environment. In addition, the FWHM of the LSPR peak can also impact the efficiency of energy transfer and coupling between plasmonic nanostructures and other systems, such as quantum emitters or photovoltaic materials. A narrower FWHM can enhance the coupling and energy transfer, leading to improved performance in applications like light-emitting devices, energy harvesting, and nanophotonic circuits. Fig. 6 shows the variation of the FWHM of ITO − Ag and GZO − Ag nanoshells calculated at various core and shell sizes while impeded in aqueous medium. This figure indicats that the shell tickness d can effectivly contrrol the FWHM of the LSPR absorption peaks of these TCO − Ag nanoshell structures. To aviod any misinterpretation of the observed variations in the simulated FWHM with the variation in core and shell sizes of TCO-Ag nanoshells due to presentation in the wavelength domain, the FWHM values are estimated from the Lorentzian fitting of the LSPR in the frequency domain as well. Similar

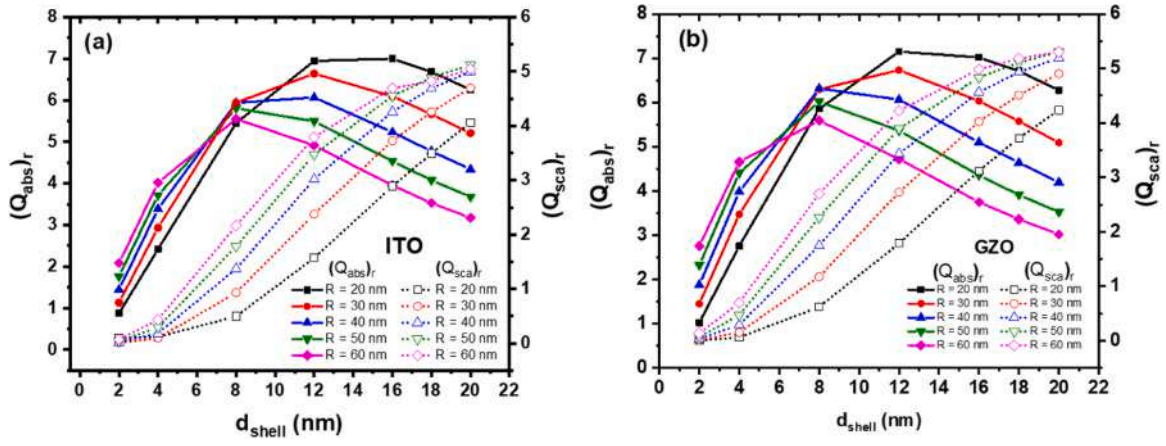

Fig. 5. The absorption and scattering intensities at resonance, $(Q_{abs})_r$ and $(Q_{sca})_r$, of TCO-Ag nanoshell with different core R_c and shell d sizes; **(a)** ITO − Ag nanoshell and **(b)** GZO − Ag nanoshell.

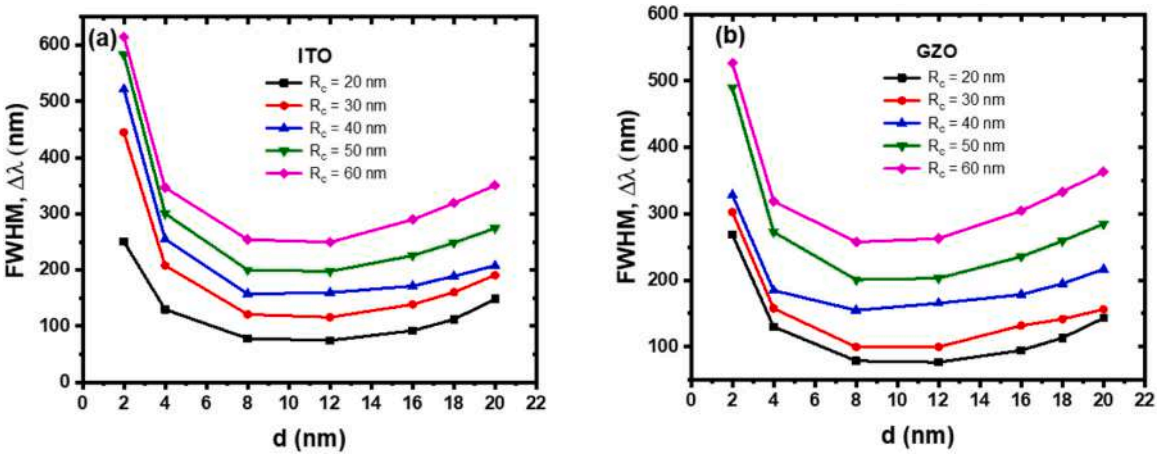

Fig. 6. The FWHM of the LSPR peaks TCO-Ag nanoshell as calculated for different core and shell sizes: **(a)** ITO − Ag nanoshell and **(b)** GZO − Ag nanoshell.

trends are observed for the variation of FWHM with geometrical paramters in both wavelength and frequency domains. However, due to our focus on the emplolyemnt of the investigated nanoshells in the applications of RIS and solar energy harvesting, we present the FWHM dependent using wavelength scale as shown in Fig. 6. The FWHM steply decreases with increasing d value from 2 to 4 nm for both TCO − Ag nanoshel structures; for ITO-Ag nanoshells it decreases to almost its half value, while for GZO-Ag nanoshells it decreases with lower rates. With further increase in d, the FWHM exhibits a minimum value between $d =$ 8 and 12nm for both TCO − Ag nanoshel structures. Afterword, the FWHM slowly increases with increasing d. This observed behavior is consistent with previously reported size dependent FWHM of several plasmonic nanostructures due to the intertwined of various LSPR damping mechanisms [3,11,65,66]. These damping mechanisms might include scattering mechanisms such as electron-surface, electron-electron, electron-lattice, and electron-phonon scattering, in addition to spontaneous radiative damping. These damping effects are customilly included within a single constant damping coefficient (Γ_0) in the dielectric functions of the core and shell materials [3,11,38]. In specific cases, the damping mechanisms of surface-scattering and radiative emission were taken to be size-dependent similar to Eq.4, thus, transitions of the FWHM from $1/r$ surface scattering dominated regime to r^3 radiative damping dominante regime were reported [65,66]. In the current study, the modified damping coefficient (Γ_{mod}) is used for Ag shells due to the significant contribution of surface scattering damping relative to its Γ_0 constant bulk damping factor. However, such damping component is found to be negligible for the TCO cores, as discussed earlier. In addition, radiative damping coefficients are taken to be constant for both TCO cores and Ag shell within the bulk value Γ_0. While the increased surface scattering damping at lower shell thickness explains the initial reduction of the FWHM with the shell thickness, the increased FWHM at higher shell thickness can be explained in terms of the increased contribution of the superimposed component of Ag plasmonic higher order modes at larger Ag shell thickness. As shown in Fig. 3, a shell thickness-dependent shoulder in the LSPR spectrum close to $\sim$ 600nm due to such multipole plasmonic resonance is observable at $d \geq$ 8nm for both ITO-Ag and GZO-Ag nanoshells. Fig. 4 also shows an increase in the FWHM of these TCO-Ag nanoshell with increasing R_c for any given shell thickness d. These results confirm the importance of the shell thickness d in controling the FWHM of these TCO-Ag nanoshell structures. Similar observation have been previously reported for CdSe- and CdTe-coated Au nanoshells [63].

In order to explore the functionality of our plasmonic TCO-Ag nanoshells for biological and chemical sensing, or even for environmental monitoring, the effect of the change in the refractive index of the surrounding medium on λ_r is investigated. The sensitivity factor S is a commonly used parameter to assess the sensing functionality of LSPR-based sensors; where S is defined as the change in λ_r relative to the change in the refractive index unit (RIU) of the surrounding medium n_{med}; i.e.; $S = d\lambda_r/dn_{med}$ [35,44,59,67–69]. However, the FWHM of the LSPR spectrum is a crucial parameter in determining the sensor functionality such that it may deteriorate or enhance the sensing and/or detecting functionality of the system. For example, it is difficult to detect small shifts in λ_r due to any change in n_{med} for wide FWHM LSPR peaks. Therefore, a Figure of Merit (FoM) factor, defined as the ratio of the sensitivity parameter S to the FWHM of the LSPR peak (FoM $= S/\Delta\lambda_{FWHM}$), is commonly used to quantify the functionality of LSPR sensors [35,44,67–69]. This FoM guarantees that the LSPR sensor concurrently addresses both requirements; high sensitivity and sharp LSPR spectrum. Fig. 7(a) and (b) show the variation of λ_r with the change in n_{med} for ITO − Ag and GZO − Ag nanoshell structures as calculated at $R_c = 60nm$ and at various values of shell thickness d. Satisfying the essential criterion for good refractive index sensing, the nanoshells exhibit consistent linear redshift in λ_r with increasing n_{med}, but with different rates depending on both R_c and d. In fact, the increase in the refractive index of the surrounding medium or core material results in a decrease in Coulombic restoring force acting between the oscillating electrons and the positive lattice, which in turn affects the light-plasmonic coupling, reduces the surface plasmon resonance energy, and shifts λ_r to longer values [68,70]. Fig. 7(c) and (d) show the variations of both S and FoM with the Ag-shell thickness for both ITO − Ag and GZO − Ag nanoshell structures. Because of the dependence of the FWHM on n_{med}, FoM calculations are performed at $n =$ 1 and $n =$ 1.33 for the two extreme investigated values of core radius, $R_c =$ 20 nm and 60nm, at different values of d. Both ITO − Ag and GZO − Ag nanoshells exhibit geometrical optimization behaviors regarding high sensitivity and great FoM, as shown in Fig. 6(c) and (d). The sensitivity S of ITO − Ag and GZO − Ag nanoshells initially show a nearly exponential decreasing behaviors with increasing d at both values of R_c. For further increase in d, the sensitivity S presents a minimum befor it starts to increase with further increase in d. Such l minmum is observed between $d =$ 8 nm and 12 nm for both TCO − Ag nanoshell structures at $R_c =$ 60nm,while it shifts to larger values of d; between 12 and 16 nm, for $R_c =$ 20 nm. The variation of the FoM factors of these TCO-Ag nanoshells with d values show inverse behaviors with broad maxima observed at $d =$ 12 nm for $R_c =$ 60 nm and at $d =$ 18 nm for $R_c =$ 20nm. At $R =$ 60 nm, ITO − Ag and GZO − Ag nanoshell structures show refractive index sensitivities ranging from $\sim$350 to $\sim$550 nm/RIU depending on the value of d. For lower core radius (R_c=20 nm), the nanoshells show lower values of S, $\sim$200 to $\sim$300 nm/RIU depending on the value of d. In any cases, these values are larger than or comparable to those of silica-Au nanoshell, a common reported nanoshell, where an $S =$

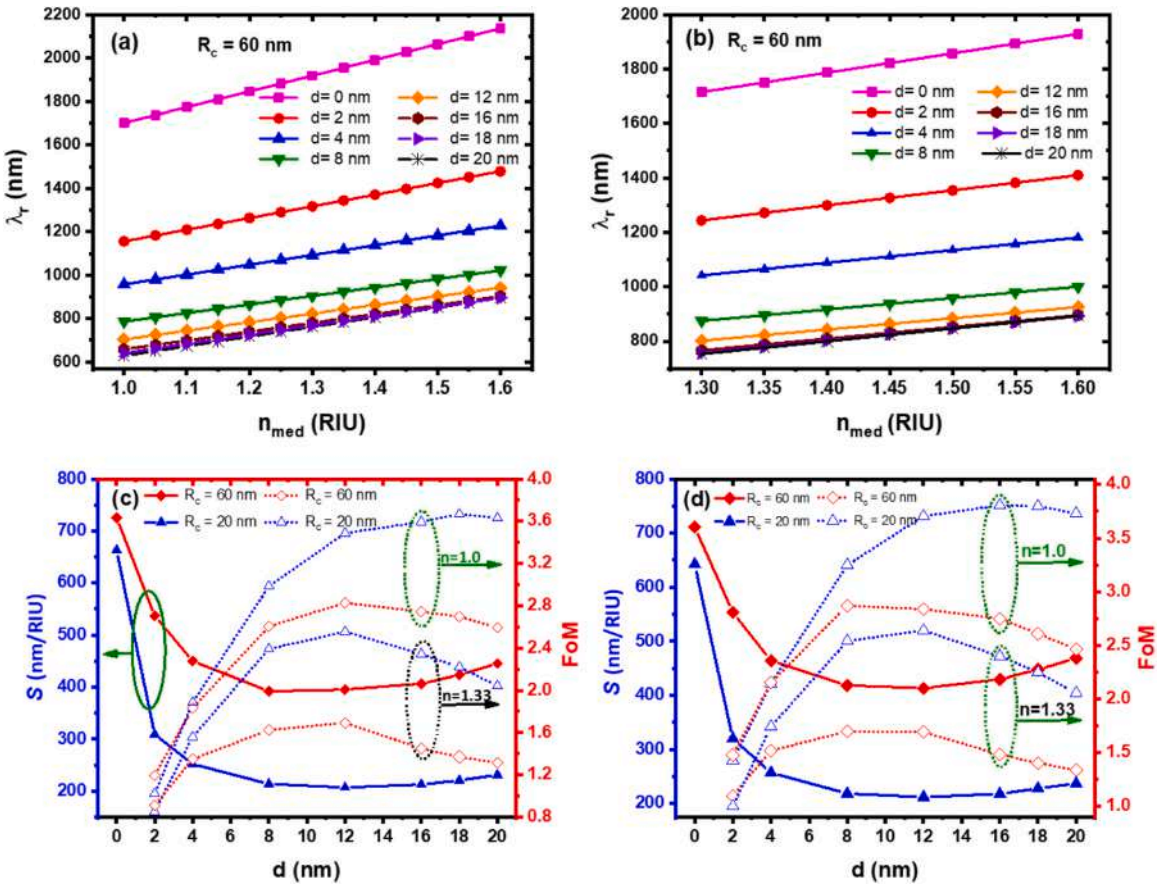

Fig. 7. Exploring the refractive index sensitivity of TCO-Ag nanoshell structures: **(a)** the variation of λ_r with n_{med} for ITO − Ag nanoshells of R_c = 60 nm and at various values of shell thickness d, **(b)** the variation of λ_r with n_{med} for GZO − Ag nanoshells of R_c =60 nm and at various values of shell thickness d, **(c)** the variation of the refractive index sensitivity S and FoM with the shell thickness d for ITO − Ag nanoshells as calculated at R_c= 20 nm and 60 nm. **(d)** the variation of the refractive index sensitivity S and FoM with the shell thickness d for GZO − Ag nanoshells as calculated at R_c= 20 nm and 60 nm.

378 nm/RIU for a 60-nm was reported. For hollow gold nanoshell, S values ranging from 250 to 550 nm/RIU were reported [71]. Using quasistatic approximation, a sensitivity S = 166 nm/RIU was reported for Au-Ag bimetallic nanoshells [72]. This indicates that these TCO-Ag nanoshells not only can provide wider tunable sensing range that extends from VIS to NIR, but high sensitivity that obviously surpass single metallic nanospheres, bimetallic nanoshells, and semiconductor-metal nanoshells [58,63,67,69,72]. At optimum geometrical conditions, ITO − Ag and GZO − Ag nanoshells present FoM values ∼2.5 and ∼3.5 for water and air surrounding medium, respectively, while presenting the minimum sensitivity. It is worth noting that ITO-Ag and GZO nanoshells have lower S values, but higher FoM values, compare to single homogenous ITO and GZO nanospheres. This is because plasmonic TCOs normally have wider LSPR than common metallic plasmonics resulted from their inherited differences associated with resonating free charge carrier's density as well as their structural and dielectric properties [6,7,73,74]. Metals, such as gold and silver, have very high free carrier concentrations (10^{22} –10^{23} electrons/cm^3), while plasmonic TCOs have much lower free carrier concentrations (10^{20} –10^{21} electrons/cm^3) [74]. Metals have lower damping rates associated only with electron-electron and electron-phonon interactions, thus narrow or sharp LSPR peaks. On the contrary, plasmonic TCOs normally have wider LSPR peaks due to higher damping rates associated with increased electron-impurity and electron-phonon scattering, in addition to higher structural and compositional inhomogeneities normally encountered in TCOs systems [73,74]. Therefore, compare to homogenous metallic or TCOs plasmonic single nanosphere, integrating TCOs cores with metallic nanoshells provides a great opportunity to control LSPR location, broadening, and enhanced RIS based on their unique inherited physical properties. In other words, a flexible geometrical optimization is always conceivable in these TCO − Ag nanoshell structure if good selectivity, high extinction, and/or high scattering are required, as is the case for many near-infrared absorption applications.

Exploiting the unique properties and capabilities of plasmonic effects e.g.; light absorption, hot electron generation and near-field enhancement, to enhance the efficiency of solar energy harvesting remains a technologically important strategy for current and future development [74,75]. Aligned with that strategy, it is valuable to perform a systematic theoretical search for optimize geometries of our current TCO-Ag plasmonic nanoshells to maximize the extinction cross-section or absorption cross-section of nanoshell structure for a desire photocatalysis or photovoltaic applications. In that regard, a figure of merit for solar energy absorption (IQ_{abs}) is used. This IQ_{abs} is defined as [76]:

$$IQ_{abs} = \int_{300nm}^{2000nm} Q_{abs}(\lambda) E_{sun}(\lambda) d\lambda \quad (7)$$

where $E_{sun}(\lambda)$ is the wavelength dependence of the sun's spectral irradiance in W/m^2.nm. Indeed, IQ_{abs} provides a reliable indicator of the ability of a given absorbing system to practically harvest solar energy throughout the essential solar radiation spectrum. Nevertheless, additional considerations must be taken in order to specifically utilize such absorbed energy in particular energy utilization channels e.g.; photovoltaic, photocatalytic, or thermal utilization [74,77]. Fig. 8 demonstrates the absorption coefficient of ITO − Ag and GZO − Ag nanoshell

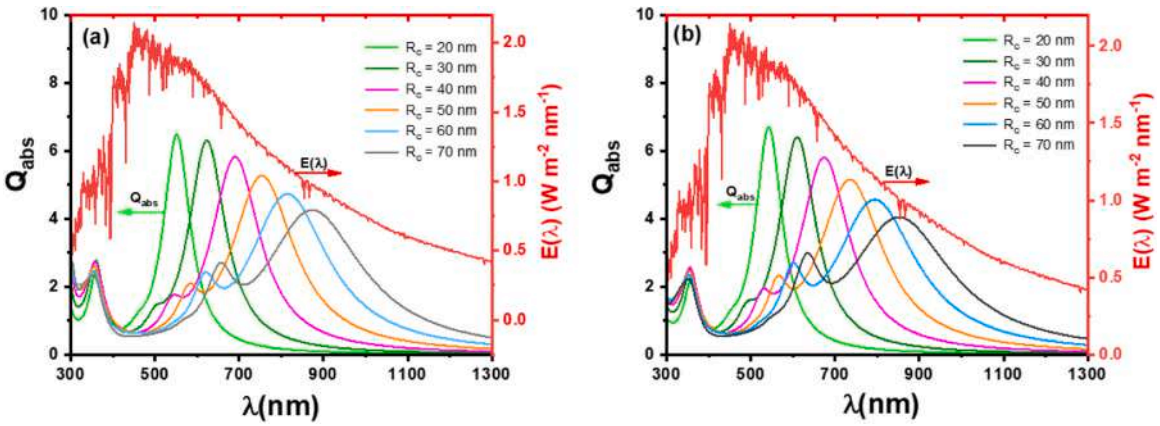

Fig. 8. The absorption coefficient of TCO-Ag nanoshell structures relative to the solar energy spectrum. The LSPR-spectrum is calculated at $d = 12$ nm and for various values of R_c assuming n=1.33: **(a)** The absorption coefficient of ITO-Ag nanoshell relative to the solar energy spectrum **(b)** The absorption coefficient of GZO-Ag nanoshell relative to the solar energy spectrum.

structures relative to the solar energy spectrum at different core size R_c = 20 −70 nm and fixed shell thickness of $d = 12$ nm. The LSPR-spectrum of ITO − Ag and GZO − Ag nanoshells can be manipulated (by varying either R_c or d or both) to coincide with any portion of the solar radiation spectrum for various potential photo-enhanced application. With the goal is to enhance solar energy absorption and utilization, it is important to have a wide LSPR spectrum that is located at wavelength of high intensity solar irradiation, which suggests using a larger TCO cores. Indeed, increasing the TCO core size widens the LSPR absorption spectrum, but shifts it to a lower intensity of solar irradiation. In contrary, increasing the metallic shell thickness shifts the LSPR spectrum to the higher solar irradiation intensity, narrows its width, and generates higher order plasmonic effects. This necessitates an optimum geometrical structure of these TCO − Ag nanoshells for energy harvesting.

Fig. 9 shows the variation of FoM for energy absorption IQ_{abs} as a function of the normalized geometrical parameter (d/R_c) for ITO − Ag and GZO − Ag nanoshell structures at different values of TCO − core radius. The calculations are performed assuming the surrounding medium to be air ($n_{med} = 1.0$) and water ($n_{med} = 1.33$), however only those for water are presented. ITO − Ag and GZO − Ag nanoshell structures show strong correlation between IQ_{abs} and the normalized geometrical parameter (d/R_c). At any given core radius R_c, the nanoshells present an utmost solar energy absorption at specific value of (d/R_c) indicating the geometry of the highest FoM for SEA for this TCO core size. At lower values of R, IQ_{abs} tends to have a broad maximum that may be extend to high values of the normalized geometrical parameter outside the investigated range i.e.; $(d/R_c) > 1$. This indicates that comparable quality of energy harvesting can be achieved via different TCO-Ag nanoshell structures having different values of normalized geometrical parameter such that $d > R_c$. This scenario remains valid for larger core sizes, up to $R_c \leq 40$ nm. Within that range, ITO − Ag and GZO − Ag nanoshells show IQ_{abs} magnitude that increases with increasing the core radius with less broad maximum trend. This suggests limited choices of TCO-Ag nanoshells of comparable energy harvesting merits regarding the optimized geometrical parameters. For TCO − Ag nanoshell structures with $R_c \geq 40$ nm, optimum energy harvesting can be only attained at specific (d/R_c) value. This behavior become more pronounced at higher values of R_c, but with a decreased maximum value of IQ_{abs}. Ultimate IQ_{abs} attaining value of ~ 1692 is observed for ITO − Ag nano shell at $R_c = 60$ nm with $d/R_c = 0.3$ geometrical structure ($d = 18nm$), while a highest IQ_{abs} value of ~ 1702 is observed for GZO − Ag nano shell at $R_c = 60$nm with $d/R_c = 0.2$ ($d = 12$ nm). For $R_c > 60$ nm, the magnitude of the maximum IQ_{abs} and its corresponding (d/R_c) value decrease with increasing R_c for the two ITO − Ag and GZO − Ag nanoshell structures. Similar trends of IQ_{abs} as a function of (d/R_c) for various values of R_c are observed for both ITO − Ag and GZO − Ag nanoshell structures assuming air surrounding medium ($n_{med} = 1.0$). The TCO − Ag shell thickness corresponding to the highest IQ_{abs} decreases with increasing core radius for both surrounding mediums. However, a blue shift relative to that of water ($n_{med} = 1.0$) of the LSPR band accompanied by a decrease in the absorption efficiency are noticeable. In addition, the magnitude of the absorption coefficient

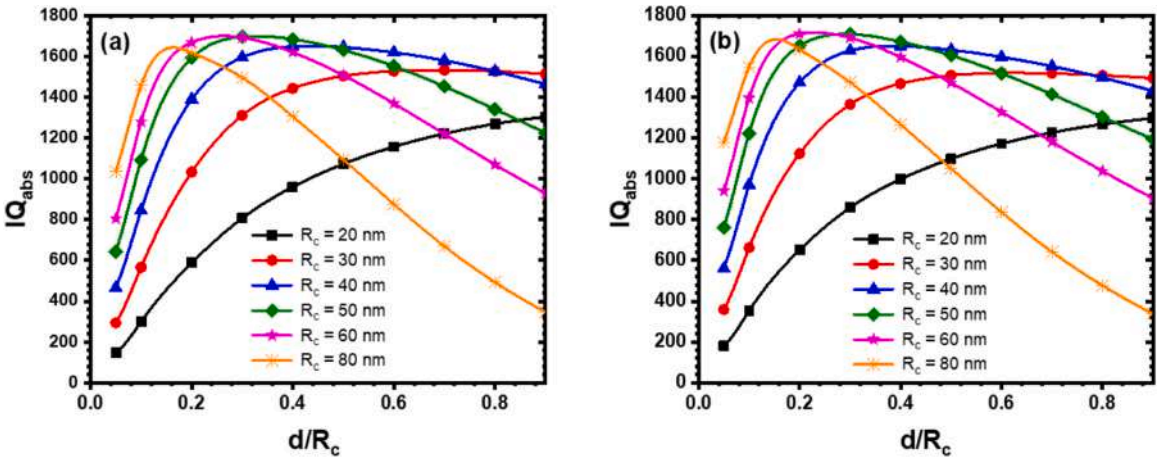

Fig. 9. The variation of the figure of merit for energy absorption IQ_{abs} of TCO-Ag nanoshells as a function of geometrical optimization parameter (d/R_c). Calculations are performed for n=1.33 of the surrounding medium. **(a)** ITO-Ag nanoshells, **(b)** GZO-Ag nanoshells.

$Q_{abs}(\lambda)$ obtained in air, and consequently IQ_{abs}, is lower than that obtained in water, but the highest FoM for energy harvesting occurs at the same (d/R_c) ratio for any given value of R_c.

4. Conclusions

In this work, the tuneability and functionality of plasmonic ITO-Ag and GZO-Ag nanoshell structures have been explored within the extended theoretical Mie theory formalism. The effect of core and shell sizes on LSPR peak position and line width as well as absorption and scattering coefficients is numerically investigated. Relative to single Ag, ITO, and GZO plasmonic nanospheres, which present limited size-dependent tunability (i.e., the tunning range $\Delta\lambda \sim 20-50$ nm as R_c increased from 10 nm to 60 nm), ITO-Ag and GZO-Ag core-shell nanostructures demonstrate tunning abilities that span from VIS to NIR with total tunning range of $\Delta\lambda \sim$ 1340 and 1170 nm, respectively. Contrary to doping and co-doping tunning mechanisms, this achieved tunning range has minimum impact on the inherited physical and chemical properties of TCO materials because it is realized by controlling its geometrical dimensions; core radius and shell thickness. Nonetheless, TCO-metal core-shell nanostructure with even wider LSPR tuning range can be accomplished by utilizing TCO cores with the highest experimentally possible carrier concentrations using doping or co-doping approaches.

Derived by its geometrically dependent LSPR spectrum, a systematic search for geometrically optimized ITO-Ag and GZO-Ag nanoshell structures with enhanced performance is performed. It is found that TCO-Ag with relatively small TCO cores and small Ag shells ($d < 12$ nm) can be utilized for absorption-based applications while those with large TCO cores and large Ag shells ($d > 12$ nm) can be utilized for scattering-based applications. In addition, the potential functionality of these nanoshell structures as RIS and SEA are examined using appropriate FoM. Simulations indicate that a geometrically optimized core-shell architecture of outstanding FoM for RIS and SEA can be realized. For $R_c = 60$ nm when $n_{med} = 1$, ITO-Ag nanoshell structures show a highest RIS sensitivity (320 −550 nm/RIU) and optimum FoM (2.8) at $d =$ 12 nm. For smaller core radius ($R_c = 20$ nm), a higher FoM and lower sensitivity are obtained at larger d value. Nearly comparable values and almost similar optimized geometrical parameters are also observed for GZO-Ag nanoshells. For $n_{med} = 1.33$, both ITO-Ag and GZO-Ag nanoshell structures show lower RIS FoM values. Furthermore, the LSPR-spectrum of ITO − Ag and GZO − Ag nanoshells can be manipulated (by varying either R or d or both) to coincide with any portion of the solar radiation spectrum to maximize its functionality for various potential photo-enhanced applications, which is estimated using FoM for energy absorption IQ_{abs}. ITO − Ag and GZO − Ag nanoshell structures show strong correlation between IQ_{abs} and the normalized geometrical parameter (d/R_c). ITO − Ag nanoshell with $R_c = 60nm$ and normalized geometrical parameter $d/R_c = 0.3$ ($d = 18$ nm) is an optimized structure of ultimate IQ_{abs} value. Optimized GZO − Ag nano shell of $R_c =$ 60 nm with $d/R_c = 0.2$ geometrical structure ($d =$ 12nm) shows a comparable utmost IQ_{abs} value of ITO − Ag nanoshells.

This work highlights the additional degree of freedom of integrating the plasmonic TCOs with noble metals into nanoshell structures to expand its tunability, optimized its functionality, and increase its adaptability. With the available varieties of TCO-core and metallic-shell material combinations, these optimized nanoshell structures can provide enhanced performance plasmonic-based devices for sensing, photocatalytic, and energy harvesting related applications.

CRediT authorship contribution statement

Hesham Fares: Writing – review & editing, Writing – original draft, Validation, Methodology, Investigation, Formal analysis, Conceptualization. **Jamal Q. M. Almarashi:** Writing – review & editing, Writing – original draft, Methodology, Investigation, Conceptualization. **Samar Moustafa:** Writing – review & editing, Writing – original draft, Methodology, Investigation, Formal analysis, Conceptualization. **Mohamed K. Zayed:** Writing – review & editing, Writing – original draft, Methodology, Investigation, Formal analysis, Data curation, Conceptualization.

Declaration of Competing Interest

The authors declare that they have no known competing financial interests or personal relationships that could have appeared to influence the work reported in this paper.

Data availability

Data will be made available on request.

References

[1] A. Gabbani, C. Sangregorio, B. Tandon, A. Nag, M. Gurioli, F. Pineider, Magneto-plasmonics beyond metals: ultrahigh sensing performance in transparent conductive oxide nanocrystals, Nano Lett. 22 (2022) 9036–9044.
[2] J. Li, Z. Lou, B. Li, Engineering plasmonic semiconductors for enhanced photocatalysis, J. Mater. Chem. A 9 (2021) 18818–18835.
[3] A. Agrawal, S.H. Cho, O. Zandi, S. Ghosh, R.W. Johns, D.J. Milliron, Localized surface plasmon resonance in semiconductor nanocrystals, Chem. Rev. 118 (2018) 3121–3207.
[4] X. Liu, M.T. Swihart, Heavily-doped colloidal semiconductor and metal oxide nanocrystals: an emerging new class of plasmonic nanomaterials, Chem. Soc. Rev. 43 (2014) 3908–3920.
[5] S. Gwo, C. Shih, Semiconductor plasmonic nanolasers: current status and perspectives, Rep. Prog. Phys. 79 (2016) 086501.
[6] G.V. Naik, A. Boltasseva, Semiconductors for plasmonics and metamaterials, Phys. Status Solidi RRL 4 (2010) 295–297.
[7] G.V. Naik, V.M. Shalaev, A. Boltasseva, Alternative plasmonic materials: beyond gold and silver, Adv. Mater. 25 (2013) 3264–3294.
[8] B. Doiron, M. Mota, M.P. Wells, R. Bower, A. Mihai, Y. Li, L.F. Cohen, N. McN. Alford, P.K. Petrov, R.F. Oulton, S.A. Maier, Quantifying figures of merit for localized surface plasmon resonance applications: a materials survey, ACS Photonics 6 (2019) 240–259.
[9] X. Ye, J. Fei, B.T. Diroll, T. Paik, C.B. Murray, Expanding the spectral tunability of plasmonic resonances in doped metal-oxide nanocrystals through cooperative cation anion codoping, J. Am. Chem. Soc. 136 (2014) 11680–11686.
[10] Y. Wang, B. Liu, Y. Wang, H. Yuan, X. Wang, X. Peng, Plasmonic semiconductor: a tunable non-metal photocatalyst, Int. J. Hydrog. Energy 46 (2021) 29858–29888.
[11] A. Agrawal, R.W. Johns, D.J. Milliron, Control of localized surface plasmon resonances in metal oxide nanocrystals, Annu. Rev. Mater. Res. 47 (2017) 1–31.
[12] M.K. Hamza, J.-M. Bluet, K. Masenelli-Varlot, B. Canut, O. Boisron, P. Melinon, B. Masenelli, Tunable mid IR plasmon in Gallium doped ZnO nanocrystals, Nanoscale 7 (2015) 12030–12037.
[13] Y. Wang, A.C. Overvig, S. Shrestha, R. Zhang, R. Wang, N. Yu, L. Negro, Tunability of indium tin oxide materials for mid-infrared plasmonics applications, Opt. Mat. Exp. 7 (2017) 2727.
[14] S. Tan, A. Argondizzo, J. Ren, L. Liu, J. Zhao, H. Petek, Plasmonic coupling at a metal/semiconductor interface, Nat. Photonics 11 (2017) 806–812.
[15] X. Liu, M.T. Swihart, Heavily-doped colloidal semiconductor and metal oxide nanocrystals: an emerging new class of plasmonic nanomaterials, Chem. Soc. Rev. 43 (2014) 3908–3920.
[16] A.K. Pradhan, R.M. Mundle, K. Santiago, J.R. Skuza, B. Xiao, K.D. Song, M. Bahoura, R. Cheaito, P.E. Hopkins, Sci. Rep. 4 (2014) 6415.
[17] R. Stanley, Plasmonics in the mid-infrared, Nat. Photonics 6 (2012) 409–411.
[18] X. Ye, J. Fei, B.T. Diroll, T. Paik, C.B. Murray, Expanding the spectral tunability of plasmonic resonances in doped metal-oxide nanocrystals through cooperative cation-anion codoping, J. Am. Chem. Soc. 136 (2014) 11680–11686.
[19] M. Kanehara, H. Koike, T. Yoshinaga, T. Teranishi, Indium tin oxide nanoparticles with compositionally tunable surface plasmon resonance frequencies in the near-IR region, J. Am. Chem. Soc. 131 (2009) 17736–17737.
[20] A.S. Kuznetsov, P. Schäfer, W. John, D. Prasai, S. Sadofev, S. Kalusniak, Enabling novel functionality in heavily doped ZnO:Ga by nanostructuring: an efficient plasmonic refractive index sensor, Nanotechnology 27 (2016) 02LT02.
[21] S.Q. Li, P. Guo, L. Zhang, W. Zhou, T.W. Odom, T. Seideman, J.B. Ketterson, R.P. H. Chang, Infrared plasmonics with indium tin-oxide nanorod arrays, ACS Nano 5 (2011) 9161–9170.
[22] K. Ma, N. Zhou, M. Yuan, D. Li, D. Yang, Tunable surface plasmon resonance frequencies of monodisperse indium tin oxide nanoparticles by controlling composition, size, and morphology, Nanoscale Res. Lett. 9 (2014) 547.
[23] E. Della Gaspera, M. Bersani, M. Cittadini, M. Guglielmi, D. Pagani, R. Noriega, S. Mehra, A. Salleo, A. Martucci, Low-temperature processed Ga-doped ZnO coatings from colloidal inks, J. Am. Chem. Soc. 135 (2013) 3439–3448.
[24] E. Della Gaspera, N.W. Duffy, J. Embden, L. Waddington, L. Bourgeois, J. J. Jasieniak, A.S.R. Chesman, Plasmonic Ge-doped ZnO nanocrystals, Chem. Commun. 51 (2015) 12369–12372.

[25] M. Yang, X. Weng, M.A. Iqbal, C. Kang, S. Zhang, Y. Zeng, Broadband photoresponse in plasmon-enhanced Ga-doped ZnO, Mater. Adv. 4 (2023) 2226.
[26] A.A. Habeeb, H. Long, L. Bao, K. Wang, B. Wang, P. Lu, Surface plasmonic resonances and enhanced IR spectra in GZO nano-triangle arrays, Mater. Lett. 172 (2016) 36–39.
[27] B. Han, L. Chen, S. Jin, S. Guo, J. Park, H.S. Yoo, J.H. Park, B. Zhao, Y.M. Jung, Modulating mechanism of the LSPR and SERS in Ag/ITO film: carrier density effect, J. Phys. Chem. Lett. 12 (31) (2021) 7612–7618.
[28] M. Sturaro, E. Della Gaspera, N. Michieli, C. Cantalini, S.M. Emamjomeh, M. Guglielmi, A. Martucci, Degenerately doped metal oxide nanocrystals as plasmonic and chemoresistive gas sensors, ACS Appl. Mater. Interfaces 8 (2016) 30440–30448.
[29] D.M. Smyth, The effects of dopants on the properties of metal oxides, Solid State Ion. 129 (2000) 5–12.
[30] S. Mahmud, S.S. Satter, A.K. Singh, M.M. Rahman, M.Y.A. Mollah, Md. Susan, Tailored engineering of bimetallic plasmonic Au@Ag Core@Shell nanoparticles, ACS Omega 4 (2019) 18061–18075.
[31] D. Wu, X. Liu, Optimization of the bimetallic gold and silver alloy nanoshell for biomedical applications in vivo, Appl. Phys. Lett. 97 (2010) 061904.
[32] T. Ghodselahi, M.A. Vesaghi, Localized surface plasmon resonance of Cu@Cu2O core–shell nanoparticles: absorption, scattering and luminescence, Phys. B 406 (2011) 2678–2683.
[33] K. Mondal, A. Sharma, Recent advances in the synthesis and application of photocatalytic metal–metal oxide core–shell nanoparticles for environmental remediation and their recycling process, RSC Adv. 6 (2016) 83589–83612.
[34] R. Kim, Z. Xu, G. Chen, D. Ma, Semiconductor and metallic core–shell nanostructures: synthesis and applications in solar cells and catalysis, Chem. Eur. J. 20 (2014) 11256–11275.
[35] F. Tam, C. Moran, N. Halas, Geometrical parameters controlling sensitivity of nanoshell plasmon resonances to changes in dielectric environment, J. Phys. Chem. B 108 (2004) 17290–17294.
[36] A.S. Kostyukov, A.E. Ershov, V.S. Gerasimov, S.A. Filimonov, I.L. Rasskazov, S. V. Karpov, Super-efficient laser hyperthermia of malignant cells with core-shell nanoparticles based on alternative plasmonic materials, J. Quant. Spectrosc. Radiat. Transf. 236 (2019) 106599.
[37] R. Hong, W. Shao, W. Sun, C. Deng, C. Tao, D. Zhang, The influence of dielectric environment on the localized surface plasmon resonance of silver-based composite thin films, Opt. Mater. 83 (2018) 212.
[38] X. Liu, B. Huang, J. Li, B. Lia, Z. Lou, Full-spectrum plasmonic semiconductors for photocatalysis (advanced article), Mater. Horiz. (2024), https://doi.org/10.1039/D4MH00515E.
[39] A. Gabbani, E.D. Latta, A. Mohan, A. Scarperi, X. Li, M. Ruggeri, F. Martini, F. Biccari, M. Kociak, M. Geppi, S. Borsacchi, F. Pineider, Direct determination of carrier parameters in indium tin oxide nanocrystals, ACS Nano 18 (23) (2024) 15139.
[40] A.L. Aden, M. Kerker, Scattering of electromagnetic waves from two concentric spheres, J. Appl. Phys. 22 (1951) 1242.
[41] M. Kerker, The Scattering of Light and Other Electromagnetic Radiation, Academic, New York, 1969.
[42] G. Mie, Contributions to the optics of turbid media, particularly of colloidal metal solutions (translation), Ann. Phys. (Weinh., Ger.) 25 (1908) 377–445.
[43] O.B. Toon, T.P. Ackerman, Algorithms for the calculation of scattering by stratified spheres, Appl. Opt. 20 (1981) 3657–3660.
[44] S. Moustafa, J.Q.M. Almarashi, M.K. Zayed, M. Almokhtar, M. Rashadd, H. Fares, Plasmon resonances of GZO core–Ag shell nanospheres, nanorods, and nanodisks for biosensing and biomedical applications in near-infrared biological windows I and II, Phys. Chem. Chem. Phys. 26 (2024) 17817–17829.
[45] C. Wu, Highly flexible touch screen panel fabricated with silver-inserted transparent ITO triple-layer structures, RSC Adv. 8 (2018) 11862–11870.
[46] Erin L. Ratcliff, A.K. Sigdel, M.R. Macech, K. Nebesny, P.A. Lee, David S. Ginley, N. R. Armstrong, J.J. Berry, Surface composition, work function, and electrochemical characteristics of gallium-doped zinc oxide, Thin Solid Films 520 (2012) 5652–5663.
[47] C. Guillén, J. Herrero, TCO/metal/TCO structures for energy and flexible electronics, Thin Solid Films 520 (2011) 1–17.
[48] J. Kim, G.V. Naik, N.K. Emani, A. Boltasseva, Plasmonic resonances in nanostructured transparent conducting oxide films, IEEE J. Sel. Top. Quantum Electron. 19 (2013) 4601907.
[49] H. Hövel, S. Fritz, A. Hilger, U. Kreibig, M. Vollmer, Width of cluster plasmon resonances: Bulk dielectric functions and chemical interface damping, Phys. Rev. B 48 (1993) 18178.
[50] P.P. Edwards, A. Porch, M.O. Jones, D.V. Morgan, R.M. Perks, Basic materials physics of transparent conducting oxides, Dalton Trans. (2004) 2995–3002.
[51] H. Hosono, K. Ueda, Transparent Conductive Oxides, in: S. Kasap, P. Capper (Eds.), Springer Handbook of Electronic and Photonic Materials, Springer Handbooks. Springer, Cham, 2017.
[52] C. Jing, J. Shi, W. Tang, The measured essentiality of electron effective mass on electron transport behavior and optical band gap in Ga-doped ZnO thin films, J. Mater. Sci. 54 (2019) 12659.
[53] J. Romann, J. Wei, M.P. Pileni, Computational matching of surface plasmon resonance: interactions between silver nanoparticles and ligands, J. Phys. Chem. C. 119 (2015) 11094–11099.
[54] A.D. Rakić, A.B. Djurišić, J.M. Elazar, M.L. Majewski, Optical properties of metallic films for vertical-cavity optoelectronic devices, Appl. Opt. 37 (1998) 5271–5283.
[55] F. Zhou, Z. Li, Y. Liu, Y. Xia, Quantitative analysis of dipole and quadrupole excitation in the surface plasmon resonance of metal nanoparticles, J. Phys. Chem. C. 112 (2008) 20233–20240.
[56] H. Long, L. Bao, A.A. Habeeb, P. Lu, Effects of doping concentration on the surface plasmonic resonances and optical nonlinearities in AGZO nanotriangle arrays, Opt. Quant. Electron 49 (2017) 345.
[57] J.K. Majhi, P.K. Kuiri, Enhancement of spectral shift of plasmon resonances in bimetallic noble metal nanoparticles in core–shell structure, J. Nanopart. Res 22 (2020) 86.
[58] R. Bardhan, N.K. Grady, T. Ali, N.J. Halas, Metallic nanoshells with semiconductor cores: optical characteristics modified by core medium properties, ACS Nano 4 (2010) 6169–6179.
[59] M.P. Navas, R.K. Soni, Laser-generated bimetallic Ag-Au and Ag-Cu core-shell nanoparticles for refractive index sensing, Plasmonics 10 (2015) 681–690.
[60] F. Enrichia, A. Quandtc, G.C. Righinia, Plasmonic enhanced solar cells: Summary of possible strategies and recent results, Renew. Sustain. Energy Rev. 82 (2018) 2433–2439.
[61] H. Choi, J. Lee, S. Ko, J. Jung, H. Park, S. Yoo, O. Park, J. Jeong, S. Park, J. Kim, Multipositional silica-coated silver nanoparticles for high-performance polymer solar cells, Nano Lett. 13 (2013) 2204–2208.
[62] J. Winans, C. Hungerford, K. Shome, L. Rothberg, P. Fauchet, Plasmonic effects in ultrathin amorphous silicon solar cells: performance improvements with Ag nanoparticles on the front, the back, and both, Opt. Express 23 (3) (2015) A92–A105.
[63] A. Bansal, S.S. Verma, Tailoring LSPR-based absorption and scattering efficiencies of semiconductor-coated Au nanoshells, Plasmonics 9 (2014) 335–341.
[64] S. Moustafa, M.K. Zayed, M. Ahmed, H. Fares, Bandwidth of quantized surface plasmons: competition between radiative and nonradiative damping effects, Phys. Chem. Chem. Phys. 26 (2024) 1994–2006.
[65] Igor Zoric, Michael Zach, Bengt Kasemo, and Christoph Langhammer, Gold, Platinum, and Aluminum Nanodisk Plasmons: Material Independence, Subradiance, and Damping Mechanisms,
[66] H. Baida, P. Billaud, S. Marhaba, D. Christofilos, E. Cottancin, A. Cru, J. Lermé, P. Maioli, M. Pellarin, M. Broyer, N. Del Fatti, F. Vallée, A. Sánchez-Iglesias, I. Pastoriza-Santos, L.M. Liz-Marzán, Quantitative determination of the size dependence of surface plasmon resonance damping in single Ag@SiO2 nanoparticles, Nano Lett. 9 (10) (2009) 3463–3469.
[67] P.K. Jain, M.A. El-Sayed, Surface plasmon resonance sensitivity of metal nanostructures: physical basis and universal scaling in metal nanoshells, J. Phys. Chem. C. 111 (2007) 17451–17454.
[68] P. Tuersun, Optimizing the figure of merit of gold nanoshell-based refractive index sensing, Optik 127 (2016) 250–253.
[69] J. Zhua, S. Zhaob, The Plasmonic refractive index sensitivity of ellipsoidal Al nanoshell: Tuning the wavelength position and width of spectral, Sens. Actuators B 232 (2016) 469–476.
[70] K. Yeneayehu, T. Senbeta, B. Mesfin, Enhancement of the optical response of Fe3O4@Ag core-shell nanoparticles, Phys. E 134 (2021) 114822.
[71] A. Steinbrück, O. Stranik, A. Csaki, W. Fritzsche, Sensoric potential of gold–silver core–shell nanoparticles, Anal. Bioanal. Chem. 401 (2011) 1241–1249.
[72] Y. Tao, Z. Guo, A. Zhang, J. Zhang, B. Wang, S. Qu, Gold nanoshells with gain-assisted silica core for ultra-sensitive biomolecular sensors, Opt. Commun. 349 (2015) 193–197.
[73] B. Tandon, A. Ashok, A. Nag, Colloidal transparent conducting oxide nanocrystals: A new infrared plasmonic material, Pramana J. Phys. 84 (2015) 087–1098.
[74] B. Yang, C. Li, Z. Wang, Q. Da, Thermoplasmonics in solar energy conversion: materials, nanostructured designs, and applications, Adv. Mater. 34 (2022) 2107351.
[75] W. Fan, M.K.H. Leung, Recent development of plasmonic resonance-based photocatalysis and photovoltaics for solar utilization, 2 -26, Molecules 21 (2016), 2 -26.
[76] M. Kumar, N. Umezawa, S. Ishii, T. Nagao, Examining the performance of refractory conductive ceramics as plasmonic materials: a theoretical approach, ACS Photonics 3 (2016) 43–50.
[77] J.G. Smith, J.A. Faucheaux, P.K. Jain, Plasmon resonances for solar energy harvesting: A mechanistic outlook, Nano Today 10 (2015) 67–80.